Materials Advances

ROYAL SOCIETY OF CHEMISTRY

PAPER

View Article Online
View Journal | View Issue

Cite this: *Mater. Adv.*, 2023, 4, 1372

Improved thermoelectric properties in n-type polycrystalline $SnSe_{0.95}$ by $PbCl_2$ doping

Xin Zhang,[ab] Jianfeng Cai,[bc] Xiaojian Tan, *[bc] Shuai Zhuang,[b] Wenjie Huang,[b] Zongwei Zhang,[b] Haoyang Hu,*[b] Jiehua Wu,[b] Guo-Qiang Liu [bc] and Jun Jiang*[bc]

Received 29th December 2022,
Accepted 6th February 2023

DOI: 10.1039/d2ma01102f

rsc.li/materials-advances

Polycrystalline tin selenide (SnSe) has attracted extensive attention because of the better mechanical performance and simpler preparation conditions than those of its single crystal. However, the low carrier concentration severely limits optimization of the thermoelectric performance, especially for n-type polycrystalline SnSe. In this work, we use the $PbCl_2$ compound as the electron dopant to prepare n-type $SnSe_{0.95}$-based materials through ball milling and hot-pressing processes. It is found that $PbCl_2$ effectively boosts the room-temperature carrier concentration from 2.6×10^{17} cm^{-3} to 5.3×10^{19} cm^{-3}. The electronic transport measurements parallel to the pressure direction indicate an enhanced power factor that increases from 0.3 μW cm^{-1} K^{-2} in pristine $SnSe_{0.95}$ to 7.3 μW cm^{-1} K^{-2} in the 6% $PbCl_2$ doped sample. The TEM images demonstrate that a large number of dislocations and grain boundaries exist in the polycrystalline, which can strengthen the phonon scattering and suppress the lattice thermal conductivity. Consequently, a maximum *ZT* of 1.13 at 823 K is obtained in the n-type $SnSe_{0.95}$ + 6% $PbCl_2$ polycrystalline parallel to the hot-pressing direction.

1. Introduction

Since most of the various energy sources are dissipated in the form of heat in human activity, there has been increasing demand to develop energy-saving technologies and improve energy efficiency.[1–3] Thermoelectric devices composed of thermoelectric materials can directly convert low-grade and distributed heat to high-grade electricity through the internal movement of charge carriers,[4–6] and are compact, pollution-free, vibration-free, noise-free, and of long life.[7] The thermoelectric conversion efficiency is dependent on the dimensionless figure of merit *ZT* of materials and the temperature difference ΔT. The *ZT* value is defined as $ZT = S^2\sigma T/\kappa$ ($\kappa = \kappa_e + \kappa_l$), where σ, S, T, κ, κ_e and κ_l represent the electrical conductivity, Seebeck coefficient, working temperature, total thermal conductivity, electronic thermal conductivity and lattice thermal conductivity, respectively.[8,9] A high *ZT* value stems from a large S and σ, and a small κ. However, the intrinsic coupling between these parameters makes it difficult to increase *ZT* significantly. Nowadays, the optimization of thermoelectric performance is mainly implemented through carrier concentration regulation,[10,11] energy band engineering,[12–15] and microstructure engineering.[16]

Tin selenide (SnSe) has not been used as a thermoelectric material for a long time. In 2014, a p-type tin selenide single crystal was prepared by Zhao *et al.* through the Bridgman method, and a maximum *ZT* value of 2.6 along the *b*-axis at 923 K was realized.[17] After that, the tin selenide compound quickly attracted widespread attention. The IV–VI compound SnSe is composed of the non-toxic and abundant elements Sn and Se, and it possesses a layered orthorhombic crystal structure.[18] The high anharmonicity resulting from the weak chemical bonds of Sn and Se promotes phonon-phonon scattering, which makes SnSe an intrinsically low thermal conductivity material.[19–21]

Although the thermoelectric property of a tin selenide single crystal is excellent, its harsh preparation conditions and weak mechanical performance of the single crystal severely limit its practical applications.[22,23] Compared with the single crystal, polycrystalline SnSe can overcome the shortcomings of the preparation process. However, the thermoelectric properties of polycrystalline SnSe are really inferior to those of the single crystal, because of the lower electrical conductivity and higher thermal conductivity.[18,24] Many efforts have been made to improve the electrical conductivity of polycrystalline SnSe. For example, K, Na, Cu, and Zn doping are adopted for the p-type polycrystalline SnSe[25–28] while Cl-, Br-, I-based dopants are used for the n-type one.[29–35] According to the progress in current research, the thermoelectric properties of n-type polycrystalline SnSe still lag behind those of the p-type materials.[11,34,36,37] Therefore, it is of important practical significance to develop high-performance n-type polycrystalline SnSe materials.

[a] *School of Material Science and Chemical Engineering, Ningbo University, Ningbo 315211, China*
[b] *Ningbo Institute of Materials Technology and Engineering, Chinese Academy of Sciences, Ningbo 315201, China. E-mail: tanxiaojian@nimte.ac.cn, huhaoyang@nimte.ac.cn, jjun@nimte.ac.cn*
[c] *University of Chinese Academy of Science, Beijing 100049, China*

In this work, we use a new halide dopant, $PbCl_2$, to adjust the carrier concentration and improve the thermoelectric properties of n-type polycrystalline SnSe by a hot-pressing method. To initiate a p–n transition in our sample, a non-isometric Sn : Se ratio of 1 : 0.95 is adopted since previous experiments showed that a 5% Se loss can induce a p–n transition in polycrystalline SnSe.[30] It is found that the $PbCl_2$ doping can effectively increase the carrier concentration and electrical conductivity. The significantly increased electrical conductivity, especially in the high temperature region, contributes to the enhanced power factor of $PbCl_2$-doped $SnSe_{0.95}$. Moreover, the induced grain boundaries and dislocation network in the sample strengthen the phonon scattering and suppress the lattice thermal conductivity. As a result, a peak ZT value of 1.13 was obtained in the n-type polycrystalline $SnSe_{0.95}$ + 6% $PbCl_2$ sample at 823 K.

2. Experimental details

Sample preparation

The high-purity raw materials Sn, Se granule (5N) and $PbCl_2$ powder (4N) were weighed according to the stoichiometric ratio of $SnSe_{0.95}$ + x mol% $PbCl_2$ (x = 0, 4, 6, 8, and 10) samples and sealed into a vacuum quartz tube (< 8 Pa). The mixture was heated and rocked in a rocking furnace at 1193 K for 1 h, then taken out and cooled in the air to room temperature. The ingots were placed into ball mill jars filled with Ar gas in a glove box, and ground in a high-energy ball mill for 5 minutes. The powders were loaded in a Φ12.7 mm graphite die and hot-pressed at 753 K under an axial pressure of 60 MPa for 10 minutes.

Characterization

A powder X-ray diffraction (XRD) analysis was applied for bulk samples parallel and perpendicular to the pressure direction by using a Bruker D8 diffractometer (Germany) with Cu K_α radiation to obtain information on the phase and crystalline orientation. The bright-field transmission electron microscopy (TEM) measurements were carried out for $SnSe_{0.95}$ + 6% $PbCl_2$ using a Talos F200x microscope to investigate the microstructures. Energy-dispersive X-ray spectroscopy (EDS) in the scanning transmission electron microscope mode was employed to illustrate the elemental distribution. The shape and orientation of grains for the x = 6 sample were observed with a Sirion 200 field-emission scanning electron microscope (SEM).

Measurement

The electrical conductivity and Seebeck coefficient of the samples with dimensions of 3 × 3 × 10 mm^{-3} were measured by an ULVAC-RIKO ZEM-3 instrument (Japan) parallel to the pressure direction with a measuring temperature range of 300–823 K under a helium atmosphere. The thermal conductivity was evaluated according to the equation $\kappa = D\rho C_p$, where D is the thermal diffusivity measured by a laser flash method (Netzsch LFA-457, Germany), ρ is the sample density obtained by the Archimedes method, and C_p is the heating capacity obtained from previous values indirectly derived in the range from room temperature to 973 K by Zhao *et al.*[17] The room-temperature Hall coefficient R_H was measured using a physical properties measurement system (Quantum Design PPMS-9, USA), and then the carrier concentration n and mobility μ were calculated by the formulae $n = 1/(eR_H)$ and $\mu = \sigma R_H$, respectively.

3. Results and discussions

Fig. 1 shows the XRD patterns of the $SnSe_{0.95}$ + x mol% $PbCl_2$ (x = 0, 4, 6, 8, and 10) samples parallel and perpendicular to the hot-pressing direction. The diffraction peaks of these samples are consistent with the standard card of orthorhombic SnSe (*Pnma* space group, PDF#48-1224) and no obvious impurities were found within the detection limits. The different intensities of the diffraction peaks parallel and perpendicular to the hot-pressing direction suggest that the obtained $SnSe_{0.95}$-based samples are structurally anisotropic. The diffraction peaks parallel to the pressure direction are mainly dominated by (111) while the diffraction peaks perpendicular to the pressure direction are mainly dominated by (400), indicating an excellent orientation. In order to determine the degree of orientation, the orientation factor of the (h00) crystalline plane, termed $F_{(h00)}$, was evaluated by the Lotgering method according to the following formulas:

$$F_{(h00)} = \frac{P - P_0}{1 - P_0}$$

$$P = \frac{\sum^{I}_{(h00)}}{\sum^{I}_{(hkl)}}, \quad P_0 = \frac{\sum^{I}_{0(h00)}}{\sum^{I}_{0(hkl)}},$$

where P and P_0 represent the ratio of the sum of diffraction intensities for the (h00) reflections to that of all the (hkl) reflections for the oriented sample and the standard PDF#48-1224 card, respectively. The closer $F_{(h00)}$ is to 1, the high texture

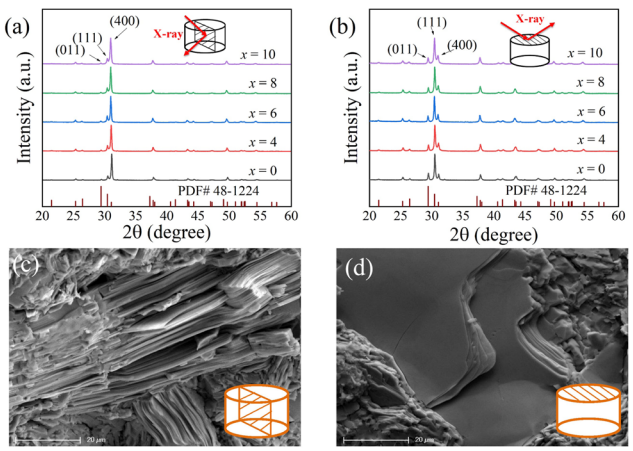

Fig. 1 The room-temperature XRD patterns of the $SnSe_{0.95}$ + x mol% $PbCl_2$ (x = 0, 4, 6, 8, and 10) samples (a) parallel and (b) perpendicular to the pressure direction. Typical SEM images of the x = 6 sample (c) parallel and (d) perpendicular to the pressure direction.

Table 1 Orientation factor $F_{(400)}$ and density ρ for the $SnSe_{0.95}$ + x mol% $PbCl_2$ (x = 0, 4, 6, 8 and 10) samples at room temperature

Sample	x = 0	x = 4	x = 6	x = 8	x = 10
$F_{(400)}$	0.41	0.48	0.45	0.49	0.46
ρ (g cm^{-3})	6.040	6.141	6.156	6.200	6.237

of the sample is like that of single crystal.[38,39] As summarized in Table 1, the $F_{(400)}$ values of the prepared $SnSe_{0.95}$ + x mol% $PbCl_2$ (x = 0, 4, 6, 8, 10) samples were 0.41, 0.48, 0.45, 0.49, and 0.46, respectively. These values are very close to that of the previously reported SnSe-based samples, indicating that our n-type $SnSe_{0.95}$ + x mol% $PbCl_2$ samples are preferentially oriented in the *bc* plane.

As investigated in the previous milestone report, n-type SnSe exhibits the out-of-plane 3D electron transport and 2D phonon transport behavior.[40] That is to say, the out-of-plane thermoelectric performance of n-type SnSe is higher than that in the *bc* plane. Considering that the oriented *bc* plane of our sample is parallel to the hot-pressing direction, in the following discussions we focus on the thermoelectric transport properties parallel to the pressure direction.

Fig. 2(a) shows the temperature-dependent electrical conductivity of the $SnSe_{0.95}$ + x mol% $PbCl_2$ (x = 0, 4, 6, 8, and 10) samples. It is found that the electrical conductivity monotonously increases with rising temperature, indicating an intrinsic semiconducting behavior.[41] Compared with the pristine $SnSe_{0.95}$, the electrical conductivities of $PbCl_2$-doped $SnSe_{0.95}$ samples are obviously improved in the measured temperature range, especially at higher temperatures (T > 650 K) owing to the thermal excitation of the carriers.[31] For instance, the electrical conductivity of the 10% $PbCl_2$-doped sample reaches

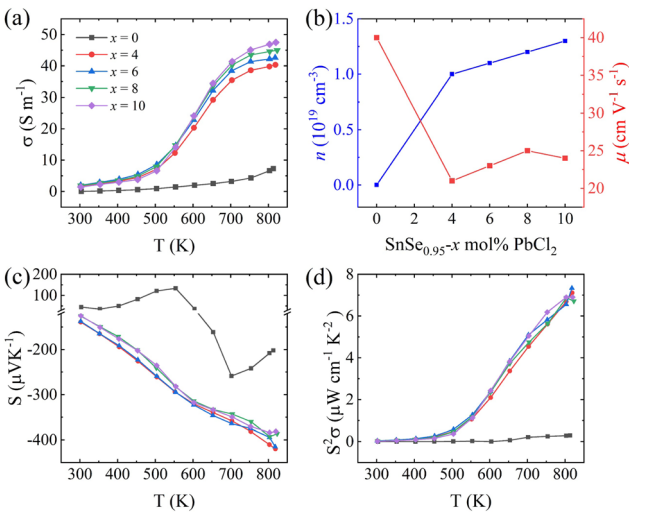

Fig. 2 Temperature dependence of the electronic transport coefficients parallel to the pressure direction for the $SnSe_{0.95}$ + x mol% $PbCl_2$ (x = 0, 4, 6, 8, and 10) sample: (a) electrical conductivity, (c) Seebeck coefficient, and (d) power factor. (b) Carrier concentration and mobility as functions of the $PbCl_2$ content at 300 K.

47.5 S cm^{-1} at 823 K, which is 5.5 times higher than that of the undoped $SnSe_{0.95}$.

As presented in Fig. 2(b), the carrier concentration significantly increases with the amount of $PbCl_2$ doping. For instance, the carrier concentration of 5.3 × 10^{19} cm^{-3} for the 10% $PbCl_2$-doped samples is 200 times more than that of the undoped $SnSe_{0.95}$ (2.6 × 10^{17} cm^{-3}). The obtained carrier concentration is much higher than those of previously reported PbSe-$SnCl_2$ co-doped samples by spark plasma sintering.[42] This observation demonstrates that Pb and Cl doping at a ratio of 1 : 2 is effective to achieve higher carrier concentrations. The variation of the room-temperature electrical conductivities of $SnSe_{0.95}$ + x mol% $PbCl_2$ samples can be explained by the changed carrier concentrations and carrier mobilities. That is, the rise of electrical conductivity from 0.03 S cm^{-1} for the undoped sample to 1.98 S cm^{-1} for the 6% $PbCl_2$-doped sample is derived from the boosted carrier concentration, and the subsequent fall to 1.42 S cm^{-1} for the 10% $PbCl_2$ doped sample is due to the decreased carrier mobility.

Fig. 2(c) shows the Seebeck coefficient *versus* temperature for the $SnSe_{0.95}$ + x mol% $PbCl_2$ (x = 0, 4, 6, 8 and 10) samples. As may be seen, the pristine $SnSe_{0.95}$ exhibits a p-type positive Seebeck coefficient at a lower temperature and an n-type negative Seebeck coefficient at a higher temperature. The p–n transition is realized in $SnSe_{0.95}$ with a 5% Se deficiency. With $PbCl_2$ doping, the Seebeck coefficients of all the $SnSe_{0.95}$ + x mol% $PbCl_2$ samples are negative, indicating an n-type conduction. The absolute values of the Seebeck coefficient of these $PbCl_2$-doped $SnSe_{0.95}$ samples monotonously increase with rising temperature. At a certain temperature, the absolute values of the Seebeck coefficient slightly decrease with the increasing $PbCl_2$ content, mainly caused by the increased carrier concentration.

The power factors of the $SnSe_{0.95}$ + x mol% $PbCl_2$ (x = 0, 4, 6, 8 and 10) samples are plotted as a function of temperature in Fig. 2(d). Owing to the increased electrical conductivity and increased absolute value of the Seebeck coefficient, the power factor significantly increases with rising temperature, especially at temperatures above 550 K. With the highest absolute value of the Seebeck coefficient and moderate electrical conductivity, the x = 6 sample exhibits the highest power factor, 7.33 μW·cm^{-1} K^{-2} at 823 K.

Fig. 3(a) shows the total thermal conductivity of the $SnSe_{0.95}$ + x mol% $PbCl_2$ (x = 0, 4, 6, 8 and 10) samples from 300 to 823 K. It is found that κ firstly decreases with rising temperature, reaches a minimum value around 750 K, and then slightly increases. The increased κ at a higher temperature may result from the excited bipolar effect, which was also found in a previous report.[43,44] At a certain temperature, κ of $PbCl_2$-doped $SnSe_{0.95}$ firstly decreases with an increasing content of $PbCl_2$, reaches a minimum value with 6% $PbCl_2$ doping, and then slightly increases. For instance, the total thermal conductivity at room temperature decreases from 1.2 W m^{-1} K^{-1} for the undoped $SnSe_{0.95}$ to 0.85 W m^{-1} K^{-1} for $SnSe_{0.95}$ + 6% $PbCl_2$.

Fig. 3(b) plots the electronic thermal conductivity as a function of temperature. κ_e is obtained according to the

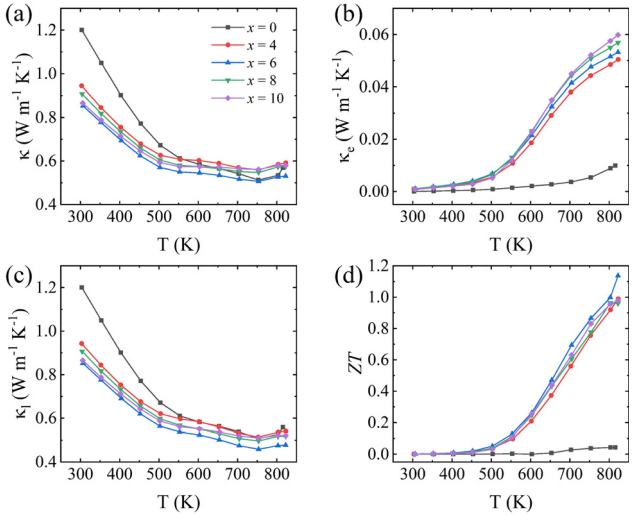

Fig. 3 Temperature-dependent (a) total thermal conductivity, (b) electronic thermal conductivity, (c) lattice thermal conductivity, and (d) *ZT* value for $SnSe_{0.95}$ + *x* mol% $PbCl_2$ (*x* = 0, 4, 6, 8, and 10) parallel to the pressure direction.

Wiedemann–Franz law, $\kappa_e = L\sigma T$, where *L* is the Lorentz constant and evaluated as $L = 1.5 + \exp(-|S|/116)$.[45] The temperature dependence of the electronic thermal conductivity is similar to that of the electrical conductivity in Fig. 2(a).

Fig. 3(c) shows the lattice thermal conductivity κ_l as a function of temperature, which is obtained by subtracting the electronic contribution κ_e from the total thermal conductivity κ. Since the electronic thermal conductivity contributes a small proportion of the total thermal conductivity, the temperature dependence of lattice thermal conductivity is almost the same as that of the total thermal conductivity. The lowest lattice thermal conductivity is 0.49 W m^{-1} K^{-1}, obtained in the 6% $PbCl_2$-doped $SnSe_{0.95}$ at 752 K. Except at temperatures higher than 750 K, the lattice thermal conductivities of the $PbCl_2$-doped $SnSe_{0.95}$ samples are lower than that of the undoped $SnSe_{0.95}$, indicating that the lead compound doping can effectively suppress the lattice thermal conductivity of tin selenide.[40]

To further explore the underlying physical mechanism of the low lattice thermal conductivity in $PbCl_2$-doped $SnSe_{0.95}$, we used a TEM technique to observe and analyze the microscopic structure of the 6% $PbCl_2$-doped sample. Fig. 4(a) is a bright-field TEM image, where grain boundaries (marked by an orange dotted line), dislocation nets (marked by a blue dotted circle), and dislocations (marked by blue triangles) can be observed. Fig. 4(b) is a high-resolution TEM of the grain boundary area marked by the white dotted box in Fig. 4(a), and it shows the orthorhombic SnSe lattice and the (400) plane with a spacing of 2.87 Å. Fig. 4(c) is an inverse fast Fourier transformation plot for the orange dotted box area in the high-resolution TEM image of Fig. 4(b), and the dislocations are marked as a red "⊥" in Fig. 4(c). A microregion quantitative EDS elemental mapping analysis was adopted to illustrate the homogeneous distribution of Sn, Pb, Cl and Se, as shown in Fig. 4(d), and is consistent with the above XRD results. Besides the point defects of $PbCl_2$ doping, the grain boundaries and induced dislocations can also enhance the phonon scattering, and they are all responsible for the suppression of the lattice thermal conductivity of $SnSe_{0.95}$-based materials.

The *ZT* values for the $SnSe_{0.95}$ + *x* mol% $PbCl_2$ (*x* = 0, 4, 6, 8, and 10) samples parallel to the pressure direction are plotted in Fig. 3(d) as a function of temperature. Since $PbCl_2$ doping boosts the carrier concentration to improve the power factor and enhances the phonon scattering to reduce the lattice thermal conductivity, all the $PbCl_2$-doped samples exhibit a higher *ZT* than that of the undoped $SnSe_{0.95}$ control sample. With the highest power factor of 7.33 μW cm^{-1} K^{-2} and lowest lattice thermal conductivity of 0.45 W m^{-1} K^{-1}, the *x* = 6 sample realizes a maximum *ZT* of 1.13 at 823 K. Although a *ZT* value of 1.13 is lower than that of the n-type $SnSe_{0.95}$ single crystal, it is still competitive with those of other polycrystalline halide-doped $SnSe_{0.95}$ systems.[11,30,46]

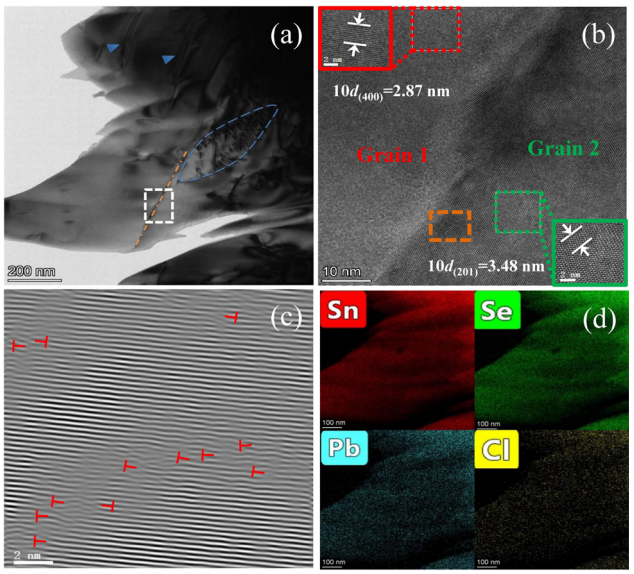

Fig. 4 TEM images for the $SnSe_{0.95}$ + 6 mol% $PbCl_2$ sample: (a) a bright-field TEM image shows grain boundaries and dislocations, (b) a high-resolution TEM image, (c) an inverse fast Fourier transformation image for the marked orange area in (b) to show the dislocations, and (d) the elemental distribution for Sn, Se, Pb, and Cl.

Conclusions

In summary, we successfully prepared the n-type polycrystalline $SnSe_{0.95}$ + *x* mol% $PbCl_2$ (*x* = 0, 4, 6, 8, and 10) samples by a hot-pressing method. The XRD result shows that the prepared samples exhibit a strong orientation along the (400) plane. The Hall measurement suggests that $PbCl_2$ is sufficient to boost the carrier concentration, leading to an obviously improved electrical conductivity and power factor. Moreover, the microstructure investigation indicates that the induced grain boundaries, dislocations, and point defects by $PbCl_2$ doping suppress the lattice thermal conductivity. As a consequence, a maximum *ZT* value of 1.13 is obtained in the $SnSe_{0.95}$ + 6% $PbCl_2$ sample.

This work provides a viable strategy for the future optimization of n-type SnSe-based thermoelectric materials.

Conflicts of interest

There are no conflicts of interest to declare.

Acknowledgements

This work was supported by the National Natural Science Foundation of China (52002382).

References

1 M. S. Dresselhaus, G. Chen, M. Y. Tang, R. G. Yang, H. Lee, D. Z. Wang, Z. F. Ren, J. P. Fleurial and P. Gogna, *Adv. Mater.*, 2007, **19**, 1043–1053.
2 X. L. Su, P. Wei, H. Li, W. Liu, Y. G. Yan, P. Li, C. Q. Su, C. J. Xie, W. Y. Zhao, P. C. Zhai, Q. J. Zhang, X. F. Tang and C. Uher, *Adv. Mater.*, 2017, **29**, 1602013.
3 Y. M. Zhou and L. D. Zhao, *Adv. Mater.*, 2017, **29**, 1702676.
4 G. J. Snyder and E. S. Toberer, *Nat. Mater.*, 2008, **7**, 105–114.
5 L. E. Bell, *Science*, 2008, **321**, 1457–1461.
6 S. B. Riffat and X. L. Ma, *Appl. Therm. Eng.*, 2003, **23**, 913–935.
7 X. Zhang and L. D. Zhao, *J. Materiomics*, 2015, **1**, 92–105.
8 L. D. Zhao, C. Chang, G. J. Tan and M. G. Kanatzidis, *Energy Environ. Sci.*, 2016, **9**, 3044–3060.
9 G. Han, Z. G. Chen, J. Drennan and J. Zou, *Small*, 2014, **10**, 2747–2765.
10 A. T. Duong, V. Q. Nguyen, G. Duvjir, V. T. Duong, S. Kwon, J. Y. Song, J. K. Lee, J. E. Lee, S. D. Park, T. Min, J. Lee, J. Kim and S. Cho, *Nat. Commun.*, 2016, **7**, 13713.
11 X. Wang, J. T. Xu, G. Q. Liu, Y. J. Fu, Z. Liu, X. J. Tan, H. Z. Shao, H. C. Jiang, T. Y. Tan and J. Jiang, *Appl. Phys. Lett.*, 2016, **108**, 083902.
12 A. Banik, U. S. Shenoy, S. Anand, U. V. Waghmare and K. Biswas, *Chem. Mater.*, 2015, **27**, 581–587.
13 M. Hong, Z. G. Chen, L. Yang, Y. C. Zou, M. S. Dargusch, H. Wang and J. Zou, *Adv. Mater.*, 2018, **30**, 1705942.
14 M. Hong, Z. G. Chen, L. Yang, T. C. Chasapis, S. D. Kang, Y. C. Zou, G. J. Auchterlonie, M. G. Kanatzidis, G. J. Snyder and J. Zou, *J. Mater. Chem. A*, 2017, **5**, 10713–10721.
15 W. Liu, X. J. Tan, K. Yin, H. J. Liu, X. F. Tang, J. Shi, Q. J. Zhang and C. Uher, *Phys. Rev. Lett.*, 2012, **108**, 166601.
16 G. J. Tan, L. D. Zhao and M. G. Kanatzidis, *Chem. Rev.*, 2016, **116**, 12123–12149.
17 L. D. Zhao, S. H. Lo, Y. S. Zhang, H. Sun, G. J. Tan, C. Uher, C. Wolverton, V. P. Dravid and M. G. Kanatzidis, *Nature*, 2014, **508**, 373–377.
18 S. Chandra, U. Bhat, P. Dutta, A. Bhardwaj, R. Datta and K. Biswas, *Adv. Mater.*, 2022, **34**, 2203725.
19 Z. G. Chen, X. L. Shi, L. D. Zhao and J. Zou, *Prog. Mater. Sci.*, 2018, **97**, 283–346.
20 C. W. Li, J. Hong, A. F. May, D. Bansal, S. Chi, T. Hong, G. Ehlers and O. Delaire, *Nat. Phys.*, 2015, **11**, 1063–1069.
21 Y. Xiao, C. Chang, Y. L. Pei, D. Wu, K. L. Peng, X. Y. Zhou, S. K. Gong, J. Q. He, Y. S. Zhang, Z. Zeng and L. D. Zhao, *Phys. Rev. B*, 2016, **94**, 125203.
22 Y. Liu, M. Calcabrini, Y. Yu, S. Lee, C. Chang, J. David, T. Ghosh, M. C. Spadaro, C. Y. Xie, O. Cojocaru-Mirédin, J. Arbiol and M. Ibáñez, *ACS Nano*, 2022, **16**, 78–88.
23 S. Chandra, P. Dutta and K. Biswas, *ACS Nano*, 2022, **16**, 7–14.
24 H. X. Liu, S. Zhang, Y. Zhang, S. T. Zong, W. Li, C. Zhu, F. Luo, J. Wang and Z. G. Sun, *ACS Appl. Energy Mater.*, 2022, **5**, 15093–15101.
25 Y. X. Chen, Z. H. Ge, M. J. Yin, D. Feng, X. Q. Huang, W. Y. Zhao and J. Q. He, *Adv. Funct. Mater.*, 2016, **26**, 6836–6845.
26 Z. H. Ge, D. S. Song, X. Y. Chong, F. S. Zheng, L. Jin, X. Qian, L. Zheng, R. E. Dunin-Borkowski, P. Qin, J. Feng and L. D. Zhao, *J. Am. Chem. Soc.*, 2017, **139**, 9714–9720.
27 J. R. Li, J. T. Xu, H. X. Wang, G. Q. Liu, X. J. Tan, H. Z. Shao, H. Y. Hu and J. Jiang, *J. Mater. Sci.: Mater. Electron.*, 2018, **29**, 18727–18732.
28 J. Liu, P. Wang, M. Y. Wang, R. Xu, J. Zhang, J. Z. Liu, D. Li, N. N. Liang, Y. W. Du, G. Chen and G. D. Tang, *Nano Energy*, 2018, **53**, 683–689.
29 G. Han, S. R. Popuri, H. F. Greer, L. F. Llin, J. G. Bos, W. Z. Zhou, D. J. Paul, H. Ménard, A. R. Knox, A. Montecucco, J. Siviter, E. A. Man, W. G. Li, M. C. Paul, M. Gao, T. Sweet, R. Freer, F. Azough, H. Baig, T. K. Mallick and D. H. Gregory, *Adv. Energy Mater.*, 2017, **7**, 1602328.
30 D. B. Li, X. J. Tan, J. T. Xu, G. Q. Liu, M. Jin, H. Z. Shao, H. J. Huang, J. F. Zhang and J. Jiang, *RSC Adv.*, 2017, **7**, 17906–17912.
31 C. Chang, Q. Tan, Y. L. Pei, Y. Xiao, X. Zhang, Y. X. Chen, L. Zheng, S. K. Gong, J. F. Li, J. Q. He and L. D. Zhao, *RSC Adv.*, 2016, **6**, 98216–98220.
32 S. Li, Y. M. Wang, C. Chen, X. F. Li, W. H. Xue, X. Y. Wang, Z. W. Zhang, F. Cao, J. H. Sui, X. J. Liu and Q. Zhang, *Adv. Sci.*, 2018, **5**, 1800598.
33 L. S. Mao, Y. N. Yin, Q. Zhang, G. Q. Liu, H. X. Wang, Z. Guo, H. Y. Hu, Y. K. Xiao, X. J. Tan and J. Jiang, *Energy Environ. Sci.*, 2020, **13**, 616–621.
34 Q. Zhang, E. K. Chere, J. Y. Sun, F. Cao, K. Dahal, S. Chen, G. Chen and Z. F. Ren, *Adv. Energy Mater.*, 2015, **5**, 1500360.
35 A. Das, A. Chauhan, V. Trivedi, M. Tiadi, R. Kumar, M. Battabyal and D. K. Satapathy, *Phys. Chem. Chem. Phys.*, 2021, **23**, 4230–4239.
36 X. L. Shi, J. Zou and Z. G. Chen, *Chem. Rev.*, 2020, **120**, 7399–7515.
37 X. Y. Mao, X. L. Shi, L. C. Zhai, W. D. Liu, Y. X. Chen, H. Gao, M. Li, D. Z. Wang, H. Wu, Z. H. Zheng, Y. F. Wang, Q. F. Liu and Z. G. Chen, *J. Mater. Sci. Technol.*, 2022, **114**, 55–61.
38 W. H. Gu, Y. X. Zhang, J. Guo, J. F. Cai, Y. K. Zhu, F. S. Zheng, L. Jin, J. T. Xu, J. Feng and Z. H. Ge, *J. Alloys Compd.*, 2021, **864**, 158401.
39 F. Li, W. T. Wang, Z. H. Ge, Z. H. Zheng, J. T. Luo, P. Fan and B. Li, *Materials*, 2018, **11**, 203–213.
40 L. Z. Su, D. Y. Wang, S. N. Wang, B. C. Qin, Y. P. Wang, Y. X. Qin, Y. Jin, C. Chang and L. D. Zhao, *Science*, 2022, **375**, 1385–1389.

41 H. X. Wang, H. Y. Hu, N. Man, C. L. Xiong, Y. K. Xiao, X. J. Tan, G. Q. Liu and J. Jiang, *Mater. Today Phys.*, 2021, **16**, 100298.
42 J. Cha, C. J. Zhou, Y. K. Lee, S. P. Cho and I. Chung, *ACS Appl. Mater. Interfaces*, 2019, **11**, 21645–21654.
43 N. Xin, Y. F. Li, H. Shen, L. Y. Shen and G. H. Tang, *J. Materiomics*, 2022, **8**, 475–488.
44 S. Chandra, U. Bhat, P. Dutta, A. Bhardwaj, R. Datta and K. Biswas, *Adv. Mater.*, 2022, **34**, 2203725.
45 J. F. Cai, Y. Zhang, Y. N. Yin, X. J. Tan, S. C. Duan, G. Q. Liu, H. Y. Hu, Y. K. Xiao, Z. H. Ge and J. Jiang, *J. Mater. Chem. C*, 2020, **8**, 13244–13252.
46 T. Shen, K. Y. Li, Z. J. Chen, H. F. Wu and J. X. Si, *J. Electron. Mater.*, 2019, **49**, 621–626.